

Fundamental and Experimental Conditions for the Realization of Traveling-Wave-Induced Aerodynamic Propulsive Forces by Piezoelectrically Deformed Plastic Substrates

Noah T. Jafferis and James C. Sturm

Abstract—In a previous work, we demonstrated the propulsive force produced by controllable traveling mechanical waves in a thin plastic sheet suspended in air above a flat surface, thus confirming the physical basis for a “flying” carpet near a horizontal surface. Here, we discuss the fundamental and experimental conditions for realizing such a demonstration. We first present the theory motivating our work and use it to determine the range of experimental conditions most likely to produce a forward propulsive force. We then present a detailed description of the experimental approach to produce the traveling waves, including integrated piezoelectric actuators and sensors to provide feedback control, artifact elimination, and power considerations. [2012-0189]

Index Terms—Actuators, aerodynamics, feedback systems, flexible structures, multisensor systems, piezoelectric devices.

I. INTRODUCTION

REFERENCE [1] presented a device that experimentally confirmed the theoretical prediction that a thin sheet vibrated in a traveling-wave shape will produce a force in the direction opposite that of the wave propagation [2], [3]. The resulting forward motion of the sheet near the ground has also been predicted to produce a lift force [4], leading to a so-called “flying” carpet [5]. This device demonstrated a form of propulsion that operates without separate moving parts since all actuation elements are formed from the same thin sheet of material. Potential advantages of this include low manufacturing costs and long lifetime. In addition, sensor arrays, e.g., chemical or biological, could be integrated onto the sheet. This device could be used to model biological organisms, e.g., for fluid dynamics studies, and is easily scalable to different sizes, provided that the operation remains in a regime of low Reynolds number. For our device, the characteristic length is set by the proximity to the ground, which is typically ~ 1 mm. This enables low Reynolds number (~ 1) operation in air, even for a relatively large (~ 10 cm) and fast-moving (~ 1 cm/s)

device (see Section II). The techniques used to produce the traveling waves, as discussed further in this work, provide local control of the shape of a thin substrate and could thus lead to a wide variety of time-varying deformations with many other applications as well, including mechanical actuators [6], speaker arrays, and adaptive optics (e.g., for telescope mirrors).

Such substrate deformation is typically achieved by applying voltages across a piezoelectric element, dielectric elastomer [7], or muscular thin film [8]. For accurate control of the shape, the ability to monitor the shape in real time with integrated deformation sensors is desirable. This is especially true for rapidly changing shapes, due to the effects of mechanical resonances and nonlinearities.

Much research has been undertaken on mechanisms for small-scale (micrometer to millimeter) propulsion, which typically takes place at relatively low Reynolds number (less than a few thousand), in three general regimes—“swimming,” “crawling,” and “flying.” For “swimming,” examples include using magnetic fields to oscillate microscopic filaments of magnetic particles in a water-based salt solution [9] (resulting in swimming velocities of ~ 10 $\mu\text{m/s}$), affixing bacteria flagella to 10- μm polystyrene beads [10] (swims at ~ 15 $\mu\text{m/s}$), and even approaches aimed at propulsion inside blood vessels, e.g., using a clinical MRI to guide a 1.5-mm magnetic bead (up to ~ 10 cm/s) in a living swine artery [11] (see [12] for an overview). In another work [13], tiny rods 5–10 mm long by 250 μm –1.5 mm wide were propelled underwater by an oscillating air bubble (propulsive forces ~ 2 –20 μN). On the centimeter scale, propulsion has been induced by periodic contraction of a “muscular thin film” in water [8], although the exact shape was not clear (velocities were still only ~ 200 $\mu\text{m/s}$). Recent works on “fish-like” swimmers (~ 10 -cm scale) have used single-actuator cantilevers made from ionic polymer metal composites [14], [15] or piezoelectrics [16] to vibrate a “tail” as a means of propulsion in water. These “fish-like” swimmers range from ~ 10 [16] to ~ 100 –300 g [14], [15] and have been propelled at ~ 2 cm/s [15] or with a ~ 20 -mN force [16]. In addition, see [17] for an overview of such devices and other actuator materials, such as shape memory alloys.

Another mechanism for small-scale propulsion is “crawling,” which is typically motivated by the motion of earthworms, such as using external magnetic fields to periodically contract

Manuscript received July 1, 2012; revised October 9, 2012; accepted October 28, 2012. Date of publication December 11, 2012; date of current version March 29, 2013. Subject Editor K. F. Bohringer.

The authors are with the Department of Electrical Engineering, Princeton University, Princeton, NJ 08544 USA, and also with the Princeton Institute for the Science and Technology of Materials, Princeton, NJ 08540 USA (e-mail: jafferis@princeton.edu; sturm@princeton.edu).

Digital Object Identifier 10.1109/JMEMS.2012.2228164

and expand a string of magnetic-fluid-containing capsules in a 12-mm tube (speed ~ 5 mm/s) [18], using shape memory alloys to periodically contract and extend (longitudinally) ~ 1 cm \times 5 cm bellows with angled “legs” to provide anisotropic friction (speed ~ 170 $\mu\text{m/s}$) [19], and a folded origami robot with a similar method of propulsion (~ 300 $\mu\text{m/s}$) [20].

Finally, small-scale propulsion in air has been an active area of research lately, from early work using an external magnetic field to rotate a ~ 5 -mm magnetized propeller [21] to the development of ~ 50 – 150 -mg flapping-wing microrobotic flies [22], [23], which use a single piezoelectric actuator to drive the wings (~ 3 -cm span) at around 100 Hz, resulting in lift forces of ~ 1 – 3 mN and a power consumption of ~ 50 mW. The Reynolds numbers for these devices are ~ 1000 – 3000 . For a more complete overview of miniature (from < 1 to ~ 15 cm) flying devices, see [24, Sec. II-C]. These flying devices are split into three categories based on lift mechanism—fixed-wing, rotating-wing, and flapping-wing. Our work is related to the “fixed-wing” category because the lift is predicted to result from the forward motion of the device. However, the mechanism of propulsion is more closely related to that of flapping devices.

Works in small-scale propulsion can be further categorized into self-propelled (i.e., the propulsion mechanism is part of the device) [8], [10], [13]–[16], [19], [20], [22], [23] and externally propelled (e.g., through the use of external magnetic fields) [9], [11], [18], [21] devices. Self-propelled devices can be more challenging due to their small size constraints (currently, they typically require connections to an external power supply) but are advantageous for reasons of autonomy and overall system-size reduction. That is, since the propulsion is generated by an onboard mechanism, rather than by an external magnetic field, for example, such devices have the potential to be completely self-contained (once a power supply can be integrated onto them). Another approach is wirelessly powered devices, such as in [25]—the actuating mechanism is still onboard, but the power is supplied wirelessly.

Our work, which is “self-propelled,” takes an approach that employs an internally generated transverse traveling-wave deformation, which is more akin to methods for under-water propulsion than to typical approaches to flight but is designed to operate in air near a boundary. This enables it to operate at Reynolds numbers less than around 10, despite its size of ~ 4 cm \times 10 cm and moving in air at speeds up to 10 cm/s (in the current work, ~ 1 -cm/s speeds have been achieved). In addition, the air boundary layer greatly reduces friction compared to “crawling,” allowing higher speeds for the same propulsive force.

In this paper, we begin by discussing the fundamental and experimental conditions under which we expect to see traveling-wave-induced propulsion in air (Section II). In Section III, we move on to the details of the experimental arrangement, including choice of material and structure, actuator and sensor operation, and removal of artifacts from the sensor signals. Section IV describes the feedback methods used to produce traveling-wave vibration in the sheet. Power considerations are discussed in Section V. Finally, we summarize our results and discuss future directions in Section VI.

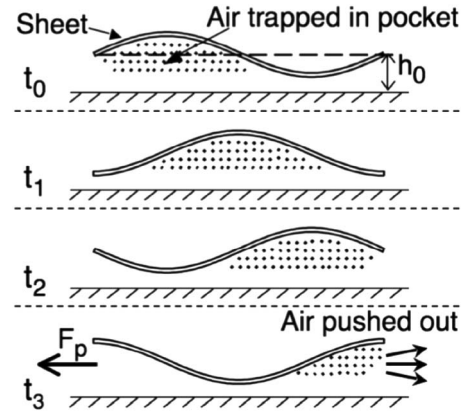


Fig. 1. Schematic diagram of a traveling-wave pump showing the shape of the sheet at a sequence of times (t_0 to t_3) over one period of oscillation. This time-varying shape pulls air in from the left and pushes it out to the right, resulting in a propulsive force F_p to the left.

II. FUNDAMENTAL MECHANISMS AND MODELING

The basic mechanism of traveling-wave-induced propulsion can be understood as follows [1]: when the sheet begins to bend in the shape of a traveling wave, a pocket of the encompassing fluid (air in our case) is pulled in from the front end and is carried along with the wave until it reaches the back end of the sheet, where it is released (Fig. 1). Thus, the traveling wave acts as a pump [26]. Since the wave acts to push fluid in the direction of the wave, there must be a corresponding force that the fluid exerts on the sheet in the direction opposite to the wave. This propulsive force is expected to increase as the gap between the sheet and the ground is decreased, due to reduced leakage on the side of the sheet that faces the ground.

The theory of [5] assumes an ideal unconstrained sheet and predicts a steady-state velocity, not a propulsive force. We desire to separate out the theoretical propulsive force because it is the intrinsic physical property of the propulsion mechanism and can therefore tell us how the system will behave if the external forces are changed (i.e., not just drag). Although the propulsion and the drag are both generated from the same piece of material (as opposed to a plane, for example, in which the propulsion is generated by an engine and the drag by the wings and body), we can separate them by assuming that the drag on the sheet when bent in a fixed sine wave shape of small amplitude is approximately equal to that of a flat sheet. Then, when the sheet's shape is changing in time, we still consider this to be the drag force, and the remaining force (in the horizontal direction) is defined to be the propulsive force. Note that we have extracted this propulsive force under the assumption that it will be unchanged by a change in the external environment (e.g., an additional restraining force); however, this would break down if the speed of the sheet were to approach the speed of the traveling wave. Since our experiments are all conducted far below this limit, we have ignored this effect in our analysis. In addition, time variations of velocity, lift height, and angle of attack are seen in the numerical simulations of [5], on the timescale of the vibration period. However, for this work, we consider much longer timescales over which we can deal with time-averaged trends, since that is what we can most easily measure in our experiments.

By comparing the theoretical steady-state velocity ν given in [5] for a free sheet with a traveling wave of given amplitude, frequency, and wavelength ($Af\lambda \sim \nu h$) to the drag force under low Reynolds number ($F_{\text{drag}} = \nu\mu_{\text{air}}WL/h$), one finds that the theoretical propulsive force induced by the wave is (see [1] for a more detailed discussion)

$$F_p \sim \frac{Af\lambda\mu_{\text{air}}WL}{h^2} \quad (1)$$

where A is the amplitude of the traveling wave, f is the frequency, λ is the wavelength, μ_{air} is the air viscosity, W is the width of the sheet, L is the length of the sheet, and h is the sheet's height above the ground. The Reynolds number is given by $\rho_{\text{air}}\nu\mathcal{L}/\mu_{\text{air}}$, where ρ_{air} is the density of the surrounding fluid (air in this case), ν is the velocity of the sheet, μ_{air} is the viscosity of air, and \mathcal{L} is a characteristic length, which is h (the height above the ground) in this scenario, provided that h is small when compared with W and L . For a sheet moving at 1 cm/s at 1 mm above the ground, this gives a Reynolds number of ~ 0.7 .

From (1), our experimental challenge is to create a thin-film traveling wave such that an observable force F_p results. However, in choosing the frequency f and amplitude A , there are several considerations and tradeoffs to be evaluated. First, we consider the physical interpretation of the sheet's "free" operation (in our experiments, the sheet is tethered—see Section III and [1] for more details—but the end goal motivating our choices is a freely moving sheet) by breaking it down into several steps A–D (equations derived from those in [5]; note that, for simplicity, we assume $\lambda = L$).

Step A: A traveling wave in the sheet pushes air backwards, resulting in a propulsive force F_p . Equation (1) is a reasonable approximation for this force provided that h is not too small [clearly, F_p cannot actually diverge as h goes to zero, as suggested by (1)] or too big (h is replaced by W or L once it becomes comparable to them) and that the vertical inertia of the sheet (due to its vibration) can be ignored. In addition, the amplitude is always limited to be less than h .

Step B: The sheet then accelerates laterally, and as it does so, it encounters two velocity-dependent forces: drag ($F_{\text{drag}} = \nu\mu_{\text{air}}WL/h$) and lift ($F_{\text{lift}} = \nu\mu_{\text{air}}WL^2/h^2$). These expressions assume low Reynolds number flow and are thus valid for small ν and h . In addition, the tilt of the sheet is assumed to be $\sim h/L$, an approximation which arises from the numerical simulations of [5].

Step C: As the sheet's lateral speed increases, the lift force increases until it is sufficient to overcome gravity, and the sheet begins to lift. The drag force increases as well, slowing the sheet's acceleration.

Step D: Since h is now increasing, the lift force decreases, as does F_p (faster than F_{drag}). Eventually, steady state is reached, in which the lift force balances gravity and the propulsive force balances the drag.

To identify promising experimental regimes in which to experimentally probe the phenomena (in air), we now look in detail at several physical regimes of operation (Fig. 2) as a

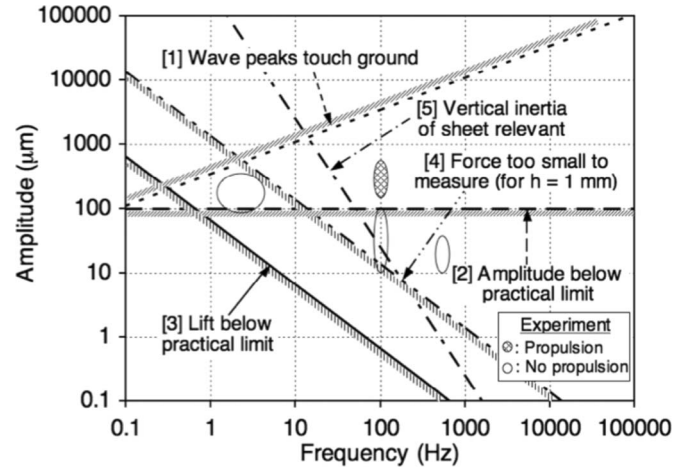


Fig. 2. Diagram depicting different physical situations as a function of amplitude and frequency of the traveling wave. The various dashed and solid lines indicate boundaries between these regimes, with the undesirable condition applying to the side with hatching. Experimental data are also shown, indicating the presence or absence of observed propulsive force in several amplitude and frequency regions.

function of the amplitude A and frequency f of the traveling wave. Some of these are relevant only for a freely moving sheet, while others are applicable in general. The physical parameters of the sheet used in this plot were length $L = 10$ cm, thickness $D = 86 \mu\text{m}$, and density $\rho = 1.77 \text{ g/cm}^3$. Five conditions were used to restrict the regimes as shown in Fig. 2.

- 1) *Wave amplitude versus lift height:* in steady state, the lift height is predicted [5] to be

$$h_{\text{steady-state}} \sim (Af)^{\frac{1}{3}} \cdot \left(\frac{\mu_{\text{air}}L^2}{\Delta\rho g D} \right)^{\frac{1}{3}} \quad (2)$$

where $\Delta\rho$ is the difference in density between the sheet and the air, g is the acceleration due to gravity, and D is the thickness of the sheet. When the traveling-wave amplitude is greater than the predicted steady-state lift height, the sheet would touch the ground on part of its oscillation and could "crawl" instead of "fly." This occurs when $A > h_{\text{steady-state}}$, which from (2) implies

$$A > \left(\frac{f\mu_{\text{air}}L^2}{\Delta\rho g D} \right)^{\frac{1}{2}} \quad (3)$$

(this condition is only relevant for a freely moving sheet, where the lift is due to aerodynamics; in our experiments, the lift is provided by external means). Equation (3) is shown as a line in Fig. 2, and the "undesirable" side of the line in amplitude-frequency space is indicated by cross-hatching.

- 2) *Average nonplanarity of sheet:* in practice, sheets made in experiments are not perfectly flat. Thus, the amplitude of vibration must be large enough to overcome any initial deviations from a perfectly flat sheet in order for the vibration shape to actually be close to that of a traveling wave. Hence, we have a lower bound on the amplitude that we can use: $A < d_{\text{ave}}$, where d_{ave} is the average

nonplanarity of the sheet. In our experiments, $d_{\text{ave}} \approx 100 \mu\text{m}$; hence, in Fig. 2, we plot

$$A < 100 \mu\text{m}. \quad (4)$$

- 3) *Maximum nonplanarity of sheet or ground*: when the sheet's forward velocity is too low, the predicted steady-state height will be less than some practical limit, determined by the maximum nonplanarity of the sheet or the ground: $h_{\text{steady-state}} < d_{\text{max}}$, where d_{max} is the maximum nonplanarity of the sheet or ground. This would result in some parts of the sheet dragging against the ground, and friction would dominate. Using (2) to substitute for $h_{\text{steady-state}}$, we obtain $(Af)^{1/3} \cdot (\mu_{\text{air}}L^2/\Delta\rho gD)^{1/3} < d_{\text{max}}$. Experimentally, $d_{\text{max}} \approx 200 \mu\text{m}$; hence, in Fig. 2, we plot

$$A \cdot f < (200 \mu\text{m})^3 \cdot \left(\frac{\Delta\rho gD}{\mu_{\text{air}}L^2} \right). \quad (5)$$

- 4) *Measurement limit*: we need to ensure that the propulsive force produced is greater than our lower measurement limit, which, for our experiments, is $\sim 10 \mu\text{N}$. Hence, by comparing this to the expression for propulsive force $F_p \sim Af\mu_{\text{air}}WL^2/h^2$, we can plot

$$A \cdot f < (10 \mu\text{N}) \cdot \left(\frac{h^2}{\mu_{\text{air}}WL^2} \right). \quad (6)$$

Note that, in this case, we have used a lift height of $h = 1 \text{ mm}$ (corresponding to our experiments), rather than the steady-state lift height $h_{\text{steady-state}}$.

- 5) *Vertical inertia*: for sufficiently high frequency and amplitude of the sheet's vibration, the vertical inertia of the sheet becomes relevant, and the actual propulsive force would be expected to be less than that predicted by (1). The onset of this effect begins essentially when the sheet's vertical acceleration is greater than gravity or

$$A \cdot f^2 > \frac{g}{4\pi^2}. \quad (7)$$

Note that this does not strongly mean that successful propulsion will not be observed, only that it might be weaker than predicted.

This analysis guides our choices for the parameters (such as A and f) used in our experiments by telling us where in parameter space should we expect the results to match the theory and what we need to do to produce propulsive forces sufficiently large to enable accurate measurement. The region outside of all of the above regions [Fig. 2; described by (3) to (7)] is the "window of operation," in which we expect to see measurable forces similar to theoretical predictions, with forces maximized at the high-frequency side. This region has a range of amplitudes from ~ 100 to $1000 \mu\text{m}$ and a range of frequencies from ~ 10 to 100 Hz . In summary, if the height h above the ground is fixed, we want to make A as large as possible, but it cannot exceed h . Reducing h is beneficial, but we can only go so far before running into practical issues (nonplanarity) as described previously. Finally, we need sufficiently high f and

A to ensure that a measurable force is produced, but going too high may not bring much benefit, due to vertical inertia.

The theoretical model presented in [5] and discussed previously assumes that we can specify the exact time-varying shape of the sheet, and predicts what will occur if that shape is a traveling wave. If actuators alone are used to drive this deformation, we would actually be providing an internal bending force, not a direct deformation, and the actual deformation would depend on the interactions with the surrounding fluid and any other external constraints. It turns out that these interactions are minor at low vibration frequencies ($< 10 \text{ Hz}$; see Section IV), but at the higher frequencies we need to operate at (~ 100 – 600 Hz), interactions between the sheet and its surroundings, and between different regions of the sheet become significant. To alleviate this issue, we use integrated sensors to measure the deformation and feedback to adjust the applied voltages as needed. There are only four of these sensors, so we still do not know the exact shape, but rather an approximation. In future versions of this work, more sensors and actuators could be added to decrease the controllable vibration wavelength.

III. EXPERIMENTAL ARRANGEMENT

Now that we have an understanding of the physics involved and the relevant regimes of operation, we proceed to the experimental implementation. Our goal is a thin sheet that can be induced to vibrate in a traveling-wave shape. We need a material that is capable of vibrating at frequencies of tens to hundreds of hertz and at amplitudes of hundreds of micrometers; hence, piezoelectrics are an attractive option. We chose polyvinylidene fluoride (PVDF) because, although its piezoelectric coefficient is not that big (23 pC/N), it is readily available in thin flexible sheets. Piezoelectrics with higher piezoelectric coefficient, such as PZT, typically need to be grown on rigid substrates, such as MgO. This limits their usefulness for "large" ($\sim 40 \text{ cm}^2$ for our samples) free-standing actuator sheets, unless they can be transferred onto a flexible substrate [27]. A standard bilayer structure (described in the following discussion) is chosen to maximize bending for a given applied voltage.

Two sheets of PVDF (Measurement-Specialties, Inc.; 1-1003702-7) are glued together with a thin epoxy layer ($t_{\text{epoxy}} \approx 30 \mu\text{m}$). Each PVDF sheet is $28 \mu\text{m}$ thick (t_{PVDF}) and is coated with 70 nm of copper and 10 nm of nickel. The metal coating on both sides of each PVDF sheet is patterned into eight regions—four of which are used as actuators (25 mm by 35 mm) and four of which are used as sensors (25 mm by 3 mm ; see [1, Fig. 2]). Loose conducting threads (diameter $\sim 50 \mu\text{m}$) are attached, using conductive epoxy, to each electrode and to the common plane between the sheets to apply and sense voltages.

The actuators operate when electric fields of opposite polarity, relative to the polarization direction, are applied across the two PVDF layers, which causes one layer to expand and the other to contract, resulting in bending [Fig. 3(a)]. The PVDF was oriented so that the coefficient of expansion was much larger in the x -direction (Fig. 3; $d_{31} = 23 \text{ pC/N}$) than in the y -direction ($d_{32} = 2.3 \text{ pC/N}$), allowing the bending to be considered unilateral. Note that this still restricts our choice of

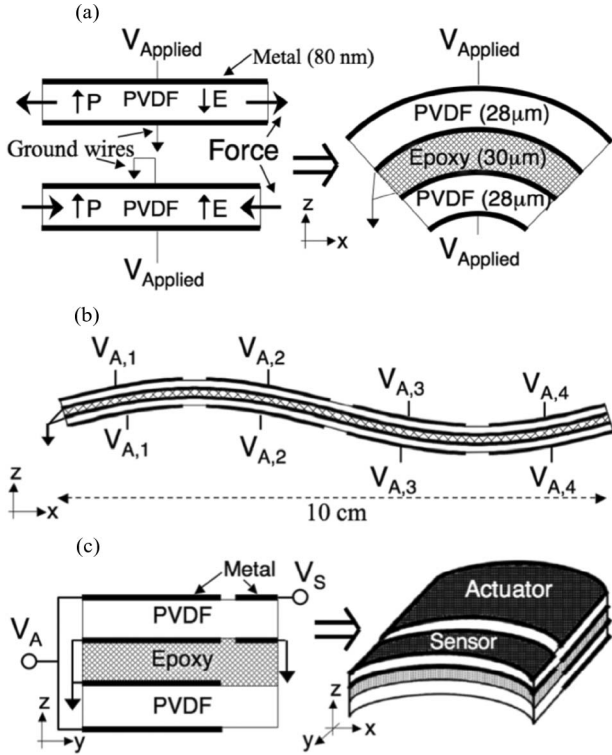


Fig. 3. Details of actuator and sensor operation. (a) Actuator cross section: the applied electric field (E) has opposite polarity with respect to the polarization (P) in the top and bottom PVDF layers, leading to opposing expansion/contraction forces and thus bending. (b) Four actuators patterned along the length of the sheet allow control of its dynamic shape. (c) Cross section showing a sensor integrated next to its corresponding actuator. Note: the sensors and actuators have separate ground terminals to minimize capacitive pickup. Since the sensor regions are relatively small, they bend along with the actuators.

the width of each actuator to be, at most, similar to its length. The normal stress in the x -direction (σ) induced in each PVDF layer (with Young's modulus $Y \approx 2$ GPa) by an applied voltage V_A is then $\sigma = d_{31}YV_A/t_{\text{PVDF}}$. For the structure shown in Fig. 3(a) (and assuming that the adhesive's Young's modulus is equal to that of the PVDF), it has been shown [28] that, for constant applied voltage, the resulting curvature $1/R$ produced by this stress is

$$\frac{1}{R} \approx \frac{12d_{31}(t_{\text{Epoxy}} + t_{\text{PVDF}})}{(t_{\text{Epoxy}} + 2t_{\text{PVDF}})^3} \cdot V_A. \quad (8)$$

We then construct a sheet with four of these actuators along its length and control the dynamic shape of the sheet by applying different time-varying voltages to each of the four actuators [Fig. 3(b)].

Piezoelectric sensors are used to measure the actual time-varying shape of the sheet, which allows the actuator control signals to be adjusted to produce a traveling wave. This step is necessary because, at higher frequencies (> 10 Hz), dynamic effects and nonlinearities cause the deformations to differ from that expected from the applied actuator voltages. The sensors are created with the same structure as the actuators but only in one of the PVDF layers to minimize the number of connections required. Because the sensors are small compared to the actuators, we assume that the curvature of each sensor is the same as the curvature of its corresponding actuator [Fig. 3(c)].

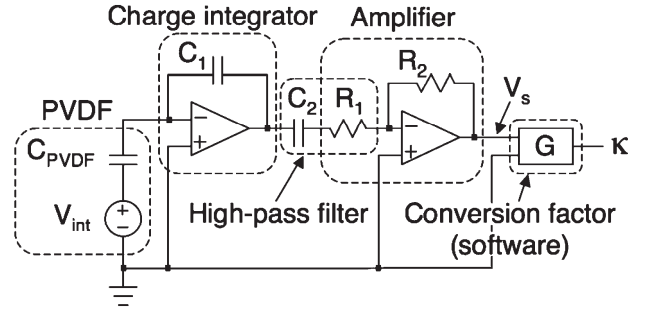


Fig. 4. Circuit diagram for measurement of sensor voltages (V_s) using charge integrator, high-pass filter, and amplifier. Curvature (κ) is calculated using software gain G .

Each sensor measures the average curvature over its area by producing an internal charge Q_{int} in the PVDF when subjected to a strain ε , given by $Q_{\text{int}}/\text{Area} = -d_{31}Y\varepsilon$. Since the PVDF is essentially a capacitor, this expression can be rewritten as $V_{\text{int}} = -d_{31}Y(t_{\text{PVDF}}/\varepsilon_0\varepsilon_r)\varepsilon$, where $\varepsilon_r \approx 13$ is the dielectric constant of the PVDF. From a simple geometric analysis, we see that, for a given curvature $1/R$, the average strain ε in the PVDF is given by $\varepsilon = (t_{\text{PVDF}} + t_{\text{Epoxy}})/2R$. Thus, we have

$$V_{\text{int}} \approx -\frac{d_{31}Y(t_{\text{PVDF}} + t_{\text{Epoxy}})t_{\text{PVDF}}}{2\varepsilon_0\varepsilon_r} \cdot \frac{1}{R}. \quad (9)$$

We use a charge integrator and amplifier circuit (Fig. 4) to measure this internal voltage, resulting in a signal $V_s = V_{\text{int}}(C_{\text{PVDF}}/C_1)(R_2/R_1)$. When V_s is multiplied by an appropriately chosen software gain $G = -(2/d_{31}Y(t_{\text{PVDF}} + t_{\text{Epoxy}})A_{\text{sensor}}) \cdot (R_1C_1/R_2) \approx 8 \text{ V}^{-1}\text{m}^{-1}$ (for our measurement circuit, $C_1 = 50$ nF, $R_1 = 10$ k Ω , $R_2 = 660$ k Ω , and the typical sensor area is ~ 0.7 cm 2), the result $\kappa = V_s \cdot G$ is numerically equal to the local curvature $1/R$. We can then construct the cross-sectional shape of the sheet as a function of time by assuming that each region has a constant curvature over its area, corresponding to the sensor measurement, and fitting together the four regions (assuming that the average height and tilt of the sheet are fixed).

Before proceeding further, we must ensure that the sensor signals result solely from the deformation-induced charge, as described previously. This is particularly crucial, given the close proximity of the actuators (applied voltages up to a few hundred volts) to the sensors (measured sensor voltages are < 1 V). To minimize capacitive pickup between the actuators and sensors, separate ground terminals are used [Fig. 3(c)]. However, this is not sufficient, as shown in Fig. 5(a): a 200-V sine wave is applied to actuator 2, and the resulting signals from all four sensors are measured. Note that, from (8) and (9), if a voltage is applied to one actuator, the signal on the corresponding sensor should have the opposite sign. Since this is not the case in Fig. 5(a), capacitive pickup from the actuator is likely still resulting in a significant artifact. To test this, the sheet is physically prevented from vibrating [Fig. 5(b)] by placing weights on the sheet, resulting in signals that are purely artifacts due to capacitive pickup from the applied voltage. Now that we know the magnitude of the artifacts (proportional to the applied voltage), we proceed to Fig. 5(c), in which these artifacts have been subtracted from the measured signals,

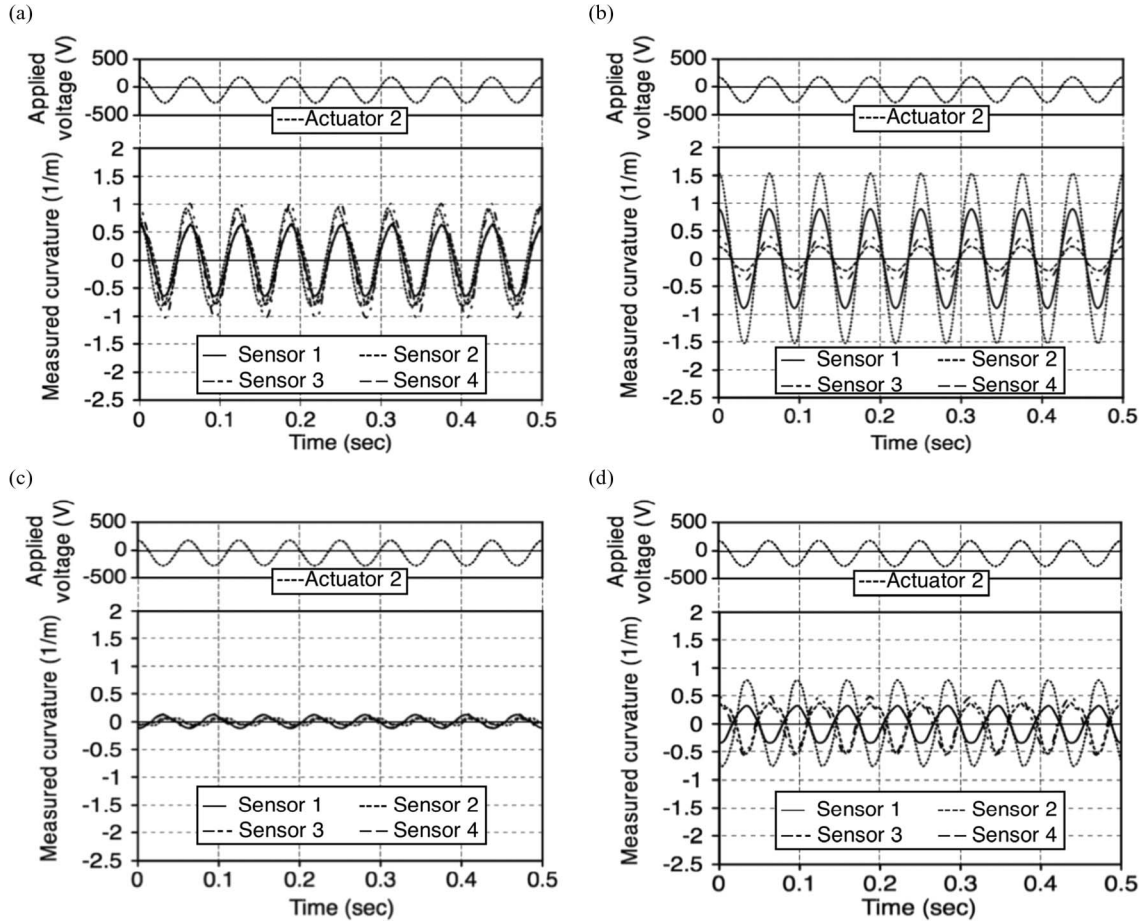


Fig. 5. Elimination of capacitive coupling—measured sensor signals are shown for a 200-V-amplitude 16-Hz sine wave applied to actuator 2. (a) Uncorrected sensor measurements. (b) Sensor measurements with a weight on the sheet to physically prevent it from vibrating, showing significant signals due to capacitive coupling. (c) Sensor signals after the software has subtracted off this artifact. (d) With the weight removed, the full true sensor signals are now observed.

resulting in sensor signals close to zero. When the weight is removed, allowing the sheet to vibrate again, the true sensor signals due to deformations can be seen [Fig. 5(d)].

Finally, due to external connections for power and control circuitry, the sheet was not entirely free, so it would not be able to reach the speeds necessary to generate its own lift (as predicted by theory [5]). Hence, two experimental arrangements were used to provide external lift (further details in [1]), both of which enable us to measure the intrinsic propulsive force produced by the traveling wave. This is because they provide a known external restoring force that acts against displacement of the sheet rather than velocity (like a pendulum), so the measurement of propulsive force can be performed at zero velocity, and hence zero drag, by measuring the steady-state displacement. In addition, we estimate the velocity by measuring the amount of time it takes for the sheet to reach the steady-state displacement. In one arrangement, the sheet is suspended from three 1-m-long threads (distinct from the conductive threads mentioned previously), which are elastic to allow the sheet the freedom to bend as desired. Experiments indicated that this setup resulted in the expected propulsive forces [1]. However, to alleviate any concerns that vibrations of the elastic threads could have an undesired impact on the results, a second arrangement was designed, in which the sheet was elevated above a miniature “air table,” so no threads were needed for suspension. In this

arrangement, the airflow of the “air table” could have had an effect on the propulsion; however, as similar results were observed in the two arrangements, we conclude that neither the suspension threads nor the airflow produced a significant effect.

IV. CONTROL OF TRAVELING-WAVE SHAPE

Some prior works have investigated mechanisms for damping vibration using arrays of piezoelectric elements, which has even been accomplished using passive electrical networks [29], [30], but for our objectives, we need more—we need to actually produce a particular desired vibration. As we will see later, we will need to dampen unwanted vibrations at other frequencies, which could be approached with a passive network; however, since we need the ability to change the desired vibration frequency and the control system for producing these vibrations is already set up, it is convenient to use the same system for canceling unwanted vibrations. The first step in attempting to control the vibration of the sheet is to determine the vibration that results from a known applied voltage waveform to each of the four actuators. Since our objective is a traveling-wave deformation, it makes sense to analyze the system in Fourier space. We proceed by first measuring a linear approximation of the system at the desired driving frequency, as described in Section IV-A. We will see that this is often not sufficient, so

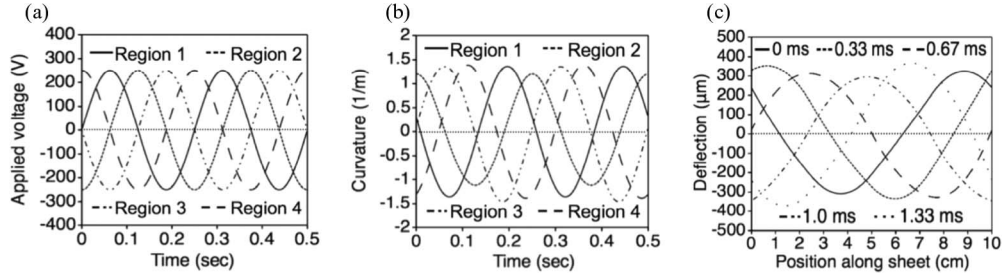


Fig. 6. At low frequencies (4 Hz in this example), applying a traveling wave of voltages is sufficient to bend the sheet in a shape close to a traveling wave. (a) Voltages applied to each region of the sheet. (b) Average curvatures as determined from the sensor readouts. (c) Reconstructed shape of the sheet at various times.

in Section IV-B, we move on to a solution using feedback to adjust the applied voltages, which allows us to proceed without needing to fully characterize the nonlinear behavior of the system. Research has been conducted on analytical and numerical simulations of wave propagation generated by a piezoelectric actuator bonded to an elastic substrate [31]; however, the conditions are somewhat different. For example, [31] considers a single actuator on an infinite (in length and thickness) substrate, in contrast to our device in which the actuators comprise most of the substrate, and there are four different interacting actuators to deal with. In addition, the external environment surrounding the sheet can involve more complicated boundary conditions (e.g., elastic thread suspension) and is often different from experiment to experiment. Together, these features make the use of integrated sensors and feedback an attractive solution.

A. Linear Control

We began our experiments by initially applying low-frequency (< 10 Hz) traveling waves of voltages to the actuators and observed through the sensors that deformations were close to the desired traveling waves (Fig. 6). However, as shown in Fig. 2, these frequencies were too low to give an observable propulsive force. At higher frequencies, dynamic effects and nonlinearities caused the deformations to be far from a traveling wave for traveling waves of voltages applied to the actuators. Fig. 7 shows an example of these measurements and demonstrates the need for integrated sensors and feedback. The left, middle, and right-hand columns show, respectively, the applied voltages, curvatures determined from the sensor voltages, and cross section of the sheet constructed from the sensor readouts. First, we show the result of applying high-frequency ($f_0 = 600$ Hz) traveling waves of voltages [Fig. 7(a)] to the actuators—the sensor signals [Fig. 7(b)] indicate that the sheet’s vibration [Fig. 7(c)] is closer to a standing wave than a traveling wave. To address this issue, a linear approximation to the relation between applied voltages and measured curvatures at a given frequency f_0 is determined by applying a sine wave of frequency f_0 to one actuator at a time and by measuring the response at each of the four sensors. Converting to Fourier space, this results in a 4×4 complex matrix

$$\mathbf{S}_{f_0} \equiv \begin{bmatrix} s_{1,1} & s_{2,1} & s_{3,1} & s_{4,1} \\ s_{1,2} & s_{2,2} & s_{3,2} & s_{4,2} \\ s_{1,3} & s_{2,3} & s_{3,3} & s_{4,3} \\ s_{1,4} & s_{2,4} & s_{3,4} & s_{4,4} \end{bmatrix} \quad (10)$$

where each coefficient $s_{j,k} = (m_k/a_j)e^{-i(\varphi_k-\phi_j)}$ corresponds to a measured signal of $m_k \cos(2\pi f_0 t + \varphi_k)$ on sensor k when a voltage $a_j \cos(2\pi f_0 t + \phi_j)$ is applied to actuator j . If the system were linear and time invariant, it would be sufficient to adjust the amplitudes and phases of the applied voltage signals, which were still sine waves of 600 Hz, according to

$$\vec{V}_{\text{Applied}} = \mathbf{S}_{f_0}^{-1} \vec{V}_{\text{Desired}} \quad (11)$$

where $\vec{V}_{\text{Applied}} \equiv [a_1 e^{-i\phi_1} \ a_2 e^{-i\phi_2} \ a_3 e^{-i\phi_3} \ a_4 e^{-i\phi_4}]$ and $\vec{V}_{\text{Desired}} \equiv [d_1 e^{-i\varphi_1} \ d_2 e^{-i\varphi_2} \ d_3 e^{-i\varphi_3} \ d_4 e^{-i\varphi_4}]$ are vectors consisting of the f_0 component of the Fourier transforms of each of the four applied voltage signals and desired sensor signals, respectively [Fig. 7(d)]. Note that, for a traveling wave, $\vec{V}_{\text{Desired}} = V_0[1 \pm i \ -1 \mp i]$. With this adjustment, some improvement is seen, but the resultant vibration [Fig. 7(f)] is still not close enough to a traveling wave—in particular, higher order vibrations can now be seen in the sensor signals [Fig. 7(e)].

B. Feedback Control

Our next step is to remove these higher order frequency modes, as well as to correct for other nonlinearities, by using feedback. We apply feedback separately for each harmonic with a “significant” undesired component present (Fig. 8), which involves first measuring the matrix \mathbf{S}_f for each frequency of interest (i.e., $f = f_0, 2f_0, 3f_0, \dots$), by the procedure described previously. Then, we apply voltages to the four actuators (beginning with zero) for ~ 1 s while measuring the response at each sensor. We then update the applied voltages according to

$$\vec{V}_{\text{Applied},f,n} = \vec{V}_{\text{Applied},f,n-1} + \mathbf{S}_f^{-1} (\vec{V}_{\text{Desired},f} - \vec{V}_{\text{Measured},f,n-1}). \quad (12)$$

Note that, for $f = f_0$, $\vec{V}_{\text{Desired},f_0} = V_0[1 \pm i \ -1 \mp i]$, while for all other harmonics, $\vec{V}_{\text{Desired},f} = 0$ for $f \neq f_0$. This feedback thus results in applied voltage waveforms [Fig. 7(g)], which now include higher frequency components, of the form

$$V_{\text{Applied},i}(t) = a_{f,i} \cos(2\pi(f)t + \phi_{f,i}) + a_{2f,i} \cos(2\pi(2f)t + \phi_{2f,i}) + \dots \quad (13)$$

With this method, we are able to cancel out all but the desired fundamental frequency of the traveling wave, as can be seen in both the sensor signals [Fig. 7(h)] and calculated cross section [Fig. 7(i)], resulting in near-ideal traveling wave.

We have also verified the traveling-wave shapes independently using a high-speed microscope camera (FC13

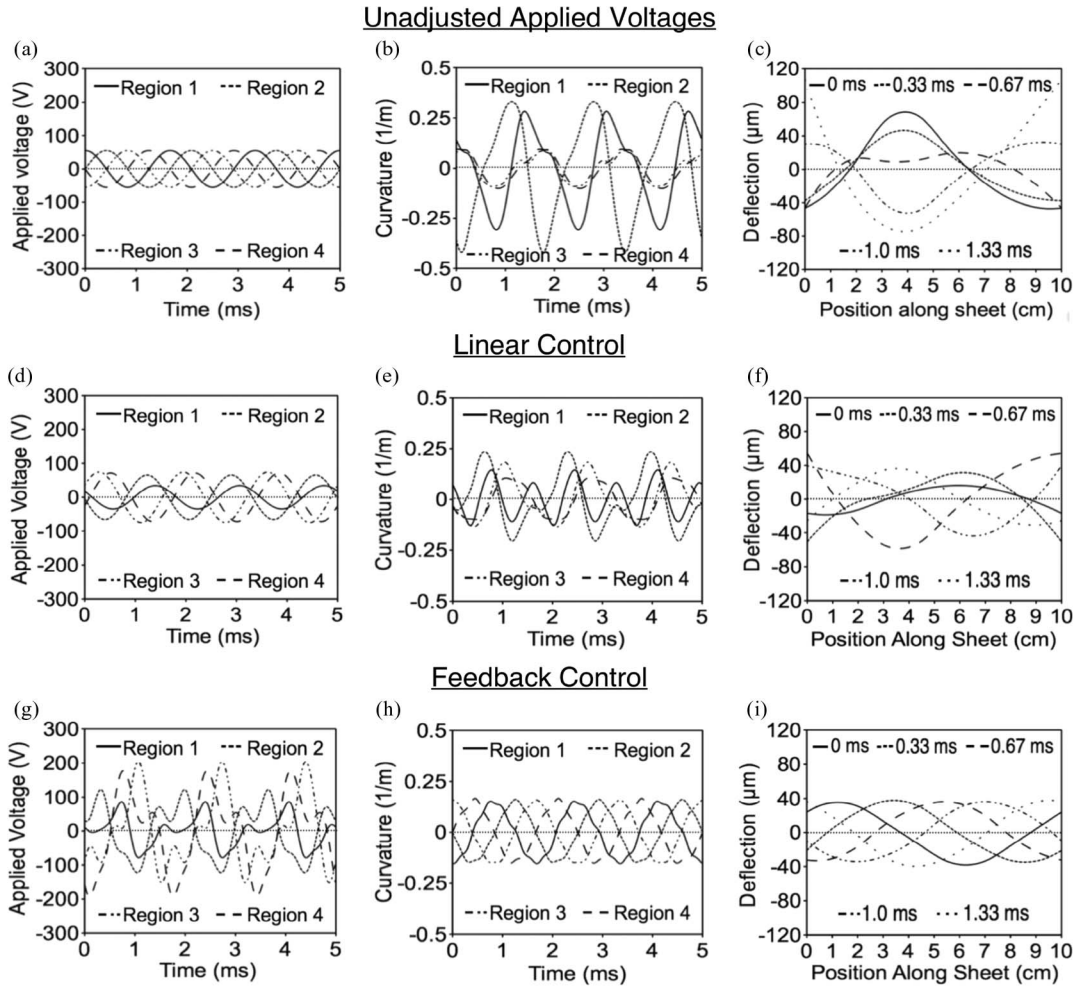


Fig. 7. Demonstration of a traveling wave, showing the significance of sensors and feedback for achieving an ideal traveling-wave shape. Data shown are at 600 Hz. The left column [plots (a), (d), and (g)] shows the applied voltages, the middle column [(b), (e), and (h)] shows the average curvatures as determined from the sensor readouts, and the right column [(c), (f), and (i)] shows the shape of the sheet at various times, as reconstructed from the sensor measurements. (a), (b), and (c) Without using sensors, the shape is close to a standing wave rather than a traveling wave. (d), (e), and (f) Applied voltages determined by the linear approximation matrix measured using sensors—shape is still not a traveling wave due to the presence of higher order modes. (g), (h), and (i) Feedback on higher order modes up to five times the fundamental needed to achieve a traveling-wave shape.

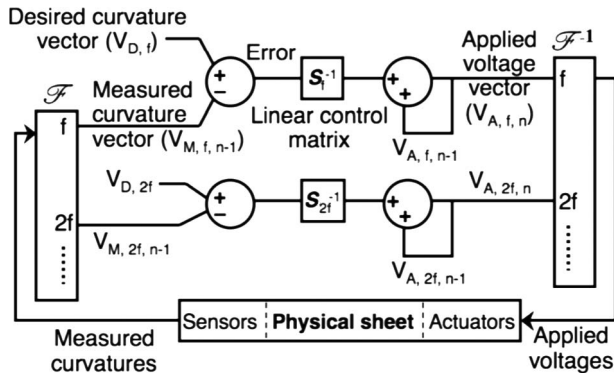


Fig. 8. Feedback block diagram. The four measured curvatures are each Fourier transformed, resulting in a curvature “vector” for each frequency component. In each feedback cycle, the applied voltage vector is updated by adding the error from the previous cycle while using the linear control matrix to ensure negative feedback. The feedback process is applied to several frequency components.

FastVision, LLC; with microscope zoom lens: final resolution of 2 μm/pixel, operated at 2000 fps) to take synchronized sequences of images (Fig. 9). This comparison is for a 100-Hz

traveling wave due to limitations on the camera’s frame rate. To achieve 2-μm resolution, the field of view was limited to ~1 mm; hence, it was necessary to take separate videos at various points along the length of the sheet (eight in this case) and to synchronize the videos to the applied voltage signals in order to re-create the entire time-varying cross section of the sheet. Simple edge-detection software was created to determine the deflection of the sheet at a given time at each location, with a precision of ~2 pixels or 4 μm. A reasonably good agreement is seen between the shape seen by the camera and the shape reconstructed from the sensor signal, considering that only four sensors are used.

With such waveforms approximating the desired traveling waves to act as an air pump, we were able to experimentally demonstrate propulsive forces and to show that they are indeed in reasonably good agreement with (1) [1]. The propulsive force reverses direction when the traveling-wave direction is reversed, drops rapidly as the sheet is raised, and increases with increasing wave amplitude. The measured propulsive forces exceed 100 μN (resulting in velocities over 1 cm/s) when the sheet is suspended ~1 mm above the ground. These propulsive

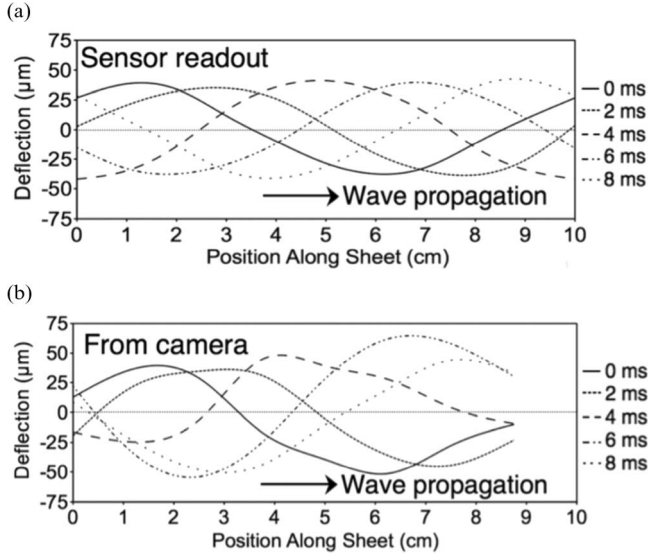


Fig. 9. Verification of the sensor readout by using synchronized sequences of images from a high-speed camera. (a) Deflection as calculated from the sensor measurements. (b) Deflection as seen in the camera images (each image taken showed a small section of the sheet at a particular time and position along its length). Image timing is synchronized to the sheet's vibration. For these measurements, the frequency of the traveling wave is 100 Hz.

forces were observed for traveling waves with a frequency of $f_0 = 100$ Hz and amplitudes of $A \approx 150\text{--}800$ μm , which falls into the expected parameter-space window (Fig. 2). Also, as expected from Fig. 2, for experiments conducted at $f_0 \approx 1\text{--}6$ Hz and $A \approx 100\text{--}400$ μm , $f_0 = 100$ Hz and $A \approx 10\text{--}100$ μm , and $f_0 = 600$ Hz and $A \approx 10\text{--}40$ μm , no propulsive force was observed.

V. POWER CONSIDERATIONS

The aerodynamic propulsive force that we have demonstrated is theoretically sufficient to achieve “flying” of the sheet, provided that it can be freed from its tethers. To achieve a truly free sheet, it will be necessary to supply onboard power. We break down the power consumption as follows: 1) given the propulsive forces that we have measured, the intrinsic power needed to propel the sheet at the steady-state velocity of ~ 20 cm/s predicted for such a propulsive force is $P_I \sim F_p * v \sim 100$ $\mu\text{N} * 20$ cm/s = $2 * 10^{-5}$ W (note, however, that our current experiments only reach ~ 1 cm/s due to the external connections, so only ~ 1 μW is needed in that case). 2) The electrical power consumed by the actuators has been directly measured to be less than 10 mW (see the following discussion) when vibrated using the same voltage amplitude and frequency as under an actuation condition predicted to produce such a velocity but with the same voltages applied to all four actuators for ease of measurement. 3) The efficiency of PVDF at converting electrical to mechanical energy can be calculated from its material properties (piezoelectric coefficient, dielectric constant, and Young's modulus) using the following equation for the maximum energy transmission coefficient λ_{\max} for a bilayer structure [32]:

$$\lambda_{\max} = \frac{32}{9k_{31}^2} \left(\sqrt{1 - k_{31}^2/4} - \sqrt{1 - 13k_{31}^2/16} \right)^2 \quad (14)$$

where k_{31} is the electromechanical coupling coefficient. This is given by $k_{31}^2 = d_{31}^2 Y / \epsilon_{33}^X$, where ϵ_{33}^X is the dielectric permittivity. For PVDF ($k_{31} \approx 0.1$), this gives $\lambda_{\max} \approx 0.3\%$ (note that other piezoelectrics can be considerably more efficient, e.g., $k_{31} \approx 0.4$ for PZT, which results in $\lambda_{\max} \approx 5\%$). For an input electrical power of 10 mW, this implies that, at most, $\sim 3 * 10^{-5}$ W is available for mechanical motion, which, to first order, agrees with the intrinsic power needed to propel the sheet at full speed. 4) The discrepancy is likely due to the energy that is lost in the interaction between the vibrating sheet and the surrounding air. The efficiency of this process has not been determined for our experiment. Note that this discrepancy could be larger, i.e., a smaller percent of power transmitted, and thus a lower efficiency for the mechanical energy to fluid energy process—if the power consumed during propulsion is greater than in the test setup. Some studies of energy harvesting from fluids [33] report energy conversion efficiency of only $\sim 0.03\%$; however, these results were found under turbulent flow conditions with considerably higher Reynolds numbers ($> 10,000$) than in our experiments (Reynolds number $\sim 1\text{--}10$). In [34], a study performed at a Reynolds number of 210 finds fluid-mechanical conversion efficiencies of $\sim 10\%$ (and in [35], $\sim 17\%$). Reference [34] also reports mechanical–electrical conversion efficiencies up to $\sim 4\%$ for PZT—this is consistent with (14), which gives $\sim 5\%$ for PZT as mentioned previously. Also, all of these studies are for conversion of fluid energy to mechanical (sheet vibration) energy, rather than mechanical to fluid as in our experiments, and thus may have somewhat different results. Supercapacitors are an attractive choice to power such a device using a boost-converter circuit, due to the need for fairly high currents. Some flexible supercapacitors (e.g., from OptiXtal) have an energy density of ~ 4 mJ/mg, which means that 1 g worth of such supercapacitors could, in principle, power the system for several minutes.

Although the required voltages and currents for our system are rather high (up to 400 V and 4 mA), the average power consumption is quite low (less than 10 mW; Fig. 10) due to the capacitive nature of the piezoelectric. The power used is determined by averaging the product of the applied voltage and current, measured as a function of time. For this measurement, the amplitude of the applied voltage was 200 V. The majority of this power (“Total Power” in Fig. 10) is actually consumed in the resistive contacts to the sheet, i.e., the conductive threads and glue (“Resistor Power” in Fig. 10)—once this effect is removed, it can be seen that the actual power consumption (“Sheet Power” in Fig. 10) is less than 10 mW for frequencies less than a few hundred hertz. Two sets of measurements are shown—one with the applied voltage updated at 10 240 updates/s and one with 102 400 updates/s. Since a lower number of updates per second implies that each step in applied voltage must be greater (for a given attempted voltage waveform) and the current is actually a series of spikes at each voltage step (since the RC time constant, which is a few microseconds, is small compared to the update period of 10 or 100 μs), the power consumed in each step in the resistive connections (which are in series with the capacitive PVDF sheet) would be expected to be ~ 100 times greater when the update rate is ten times greater, so the average power consumed in the resistor would be ~ 10 times greater. Of

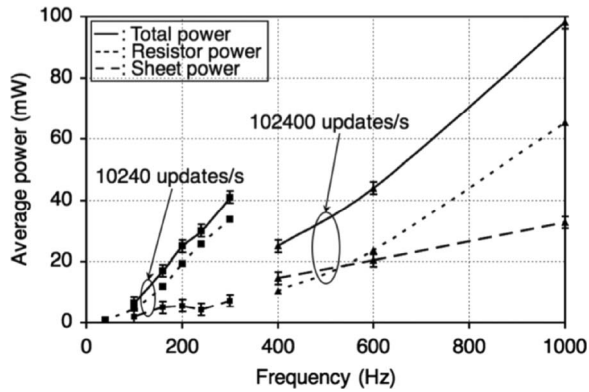


Fig. 10. Average power consumption of the sheet. Two sets of measurements are shown—one with the applied voltage updated at 10 240 times/s and one with 102 400 times/s. After the power lost in the resistive contacts ($\sim 250 \Omega$ in this case) is removed, both measurements give similar average power consumption by the sheet itself.

course, this assumes that the current decays completely before the next voltage step, which is not exactly valid for the 102 400-updates/s case. Hence, while we do, in fact, see a larger “resistor power” for the 102 400-updates/s case, it is ~ 5 to 8 times larger than the 10 240-updates/s case, rather than ten times.

VI. SUMMARY AND FUTURE DIRECTIONS

In summary, we have identified theoretical and practical considerations that are used to guide our choice of parameters for the investigation of propulsive forces produced by traveling waves in thin sheets of material and chose the materials and structure necessary to meet these criteria. We then showed how integrated sensors are used to adjust the actuator signals using linear control matrices and feedback, which resulted in near-ideal traveling-wave shapes.

A clear future challenge would be to develop an onboard power supply within the size and weight constraints, e.g., less than the weight of the sheet. This might be accomplished with thin-film batteries or supercapacitors. Alternatively, by using a more efficient piezoelectric, such as PZT nanoribbons on plastic [27], the necessary voltages would be greatly reduced, and larger amplitudes would be possible, providing a clear direction for future work.

REFERENCES

- [1] N. T. Jafferis, H. A. Stone, and J. C. Sturm, “Traveling wave-induced aerodynamic propulsive forces using piezoelectrically deformed substrates,” *Appl. Phys. Lett.*, vol. 99, no. 11, pp. 114102-1–114102-3, Sep. 2011.
- [2] G. Taylor, “Analysis of the swimming of microscopic organisms,” *Proc. R. Soc. Lond. A, Math. Phys. Sci.*, vol. 209, no. 1099, pp. 447–461, Nov. 1951.
- [3] A. J. Reynolds, “The swimming of minute organisms,” *J. Fluid Mech.*, vol. 23, no. 2, pp. 241–360, Oct. 1965.
- [4] G. Taylor, “Film notes for low-Reynolds-number flows,” Nat. Committee Fluid Mech. Films, Cambridge, MA, No. 21617, 1967.
- [5] M. Argentina, J. Skotheim, and L. Mahadevan, “Settling and swimming of flexible fluid-lubricated foils,” *Phys. Rev. Lett.*, vol. 99, no. 22, pp. 224503-1–224503-4, Nov. 2007.
- [6] S. Tuncdemir, S. O. Ural, and K. Uchino, “Meso-scale piezoelectric gripper with high dexterity,” *Jpn. J. Appl. Phys.*, vol. 48, no. 4, pp. 044501-1–044501-8, Apr. 2009.
- [7] R. Pelrine, R. Kornbluh, Q. Pei, and J. Joseph, “High-speed electrically actuated elastomers with strain greater than 100%,” *Science*, vol. 287, no. 5454, pp. 836–839, Feb. 2000.
- [8] A. W. Feinberg, A. Feigel, S. S. Shevkoplyas, S. Sheehy, G. M. Whitesides, and K. K. Parker, “Muscular thin films for building actuators and powering devices,” *Science*, vol. 317, no. 5843, pp. 1366–1370, Sep. 2007.
- [9] R. Dreyfus, J. Baudry, M. L. Roper, M. Fermigier, H. A. Stone, and J. Bibette, “Microscopic artificial swimmers,” *Nature*, vol. 437, no. 7060, pp. 862–865, Oct. 2005.
- [10] B. Behkam and M. Sitti, “Bacterial flagella-based propulsion and on/off motion control of microscale objects,” *Appl. Phys. Lett.*, vol. 90, no. 2, pp. 023902-1–023902-3, Jan. 2007.
- [11] S. Martel, J.-B. Mathieu, O. Felfoul, A. Chanu, É. Aboussouan, S. Tamaz, P. Poupponeau, G. Beaudoin, G. Soulez, L. H. Yahia, and M. Mankiewicz, “Automatic navigation of an untethered device in the artery of a living animal using a conventional clinical magnetic resonance imaging system,” *Appl. Phys. Lett.*, vol. 90, no. 11, pp. 114105-1–114105-3, Mar. 2007.
- [12] S. Martel, “Collective methods of propulsion and steering for untethered microscale nanorobots navigating in the human vascular network,” *Proc. Inst. Mech. Eng. Mech. Eng. Sci.*, vol. 224, no. 7, pp. 1505–1513, Jul. 2010.
- [13] K. Ryu, J. Zueger, S. K. Chung, and S. K. Cho, “Underwater propulsion using ac-electrowetting-actuated oscillating bubbles for swimming robots,” in *Proc. IEEE 23rd Int. Conf. MEMS*, 2010, pp. 160–163.
- [14] M. Aureli, V. Kopman, and M. Porfiri, “Free-locomotion of underwater vehicles actuated by ionic polymer metal composites,” *IEEE/ASME Trans. Mechatronics*, vol. 15, no. 4, pp. 603–614, Aug. 2010.
- [15] Z. Chen, S. Shatarra, and X. Tan, “Modeling of biomimetic robotic fish propelled by an ionic polymer-metal composite caudal fin,” *IEEE/ASME Trans. Mechatronics*, vol. 15, no. 3, pp. 448–459, Jun. 2010.
- [16] A. Erturk and G. Delporte, “Underwater thrust and power generation using flexible piezoelectric composites: An experimental investigation toward self-powered swimmer-sensor platforms,” *Smart Mater. Struct.*, vol. 20, no. 12, pp. 125013-1–125013-11, Dec. 2011.
- [17] W.-S. Chu, K.-T. Lee, S.-H. Song, M.-W. Han, J.-Y. Lee, H.-S. Kim, M.-S. Kim, Y.-J. Park, K.-J. Cho, and S.-H. Ahn, “Review of biomimetic underwater robots using smart actuators,” *Int. J. Precision Eng. Manuf.*, vol. 13, no. 7, pp. 1281–1292, Jul. 2012.
- [18] N. Saga and T. Nakamura, “Development of a peristaltic crawling robot using magnetic fluid on the basis of the locomotion mechanism of the earthworm,” *Smart Mater. Struct.*, vol. 13, no. 3, pp. 566–569, Jun. 2004.
- [19] B. Kim, M. G. Lee, Y. P. Lee, Y. Kim, and G. Lee, “An earthworm-like micro robot using shape memory alloy actuator,” *Sens. Actuators A, Phys.*, vol. 125, no. 2, pp. 429–437, Jan. 2006.
- [20] C. D. Onal, R. J. Wood, and D. Rus, “Towards printable robotics: Origami-inspired planar fabrication of three-dimensional mechanisms,” in *Proc. IEEE Int. Conf. Robot. Autom.*, 2011, pp. 4608–4613.
- [21] N. Miki and I. Shimoyama, “Analysis of the flight performance of small magnetic rotating wings for use in microrobots,” in *Proc. IEEE Int. Conf. Robot. Autom.*, 1998, pp. 3065–3070.
- [22] R. J. Wood, “The first takeoff of a biologically inspired at-scale robotic insect,” *IEEE Trans. Robot.*, vol. 24, no. 2, pp. 341–347, Apr. 2008.
- [23] R. J. Wood, B. Finio, M. Karpelson, N. O. Pérez-Arancibia, P. Sreetharan, and J. P. Whitney, “Challenges for micro-scale flapping-wing micro air vehicles,” in *Proc. SPIE*, 2012, vol. 8373, pp. 83731J-1–83731J-9.
- [24] N. R. Coleman, “Micro-scale flapping wings for the advancement of flying MEMS,” M.S. thesis, Air Force Inst. of Tech., Wright-Patterson Air Force Base, OH, 2009.
- [25] K. Abdelnour, A. Stinchcombe, and M. Porfiri, “Wireless powering of ionic polymer metal composites toward hovering microswimmers,” *IEEE/ASME Trans. Mechatronics*, vol. 17, no. 5, pp. 924–935, Oct. 2012.
- [26] K. P. Selverov and H. A. Stone, “Peristaltically driven channel flows with applications toward micromixing,” *Phys. Fluids*, vol. 13, no. 7, pp. 1837–1859, Jul. 2001.
- [27] Y. Qi, N. T. Jafferis, K. Lyons, Jr., C. M. Lee, H. Ahmad, and M. C. McAlpine, “Piezoelectric ribbons printed onto rubber for flexible energy conversion,” *Nano Lett.*, vol. 10, no. 2, pp. 524–528, Feb. 2010.
- [28] J. D. Ervin and D. Brei, “Recurve piezoelectric-strain-amplifying actuator architecture,” *IEEE/ASME Trans. Mechatronics*, vol. 3, no. 4, pp. 293–301, Dec. 1998.
- [29] F. dell’Isola, M. Porfiri, and S. Vidoli, “Piezo-ElectroMechanical (PEM) structures: Passive vibration control using distributed piezoelectric transducers,” *Comp. Rendus Mecanique*, vol. 331, no. 1, pp. 69–76, Dec. 2003.
- [30] F. Casadei, M. Ruzzene, L. Dozio, and K. A. Cunefare, “Broad-band vibration control through periodic arrays of resonant shunts: Experimental investigation on plates,” *Smart Mater. Struct.*, vol. 19, no. 1, pp. 015002-1–015002-13, Jan. 2010.

- [31] G. L. Huang and C. T. Sun, "The dynamic behavior of a piezoelectric actuator bonded to an anisotropic elastic medium," *Int. J. Solids Struct.*, vol. 43, no. 5, pp. 1291–1307, Mar. 2006.
- [32] Q.-M. Wang, X.-H. Du, B. Xu, and L. E. Cross, "Electromechanical coupling and output efficiency of piezoelectric bending actuators," *IEEE Trans. Ultrason., Ferroelectr., Freq. Control*, vol. 46, no. 3, pp. 638–646, May 1999.
- [33] H. D. Akaydin, N. Elvin, and Y. Andreopoulos, "Energy harvesting from highly unsteady fluid flows using piezoelectric materials," *J. Intell. Mater. Syst. Struct.*, vol. 21, no. 13, pp. 1263–1278, Sep. 2010.
- [34] D. T. Akcabay and Y. L. Young, "Hydroelastic response and energy harvesting potential of flexible piezoelectric beams in viscous flow," *Phys. Fluids*, vol. 24, no. 5, pp. 054106-1–054106-19, May 2012.
- [35] J. A. Dunnmon, S. C. Stanton, B. P. Mann, and E. H. Dowell, "Power extraction from aeroelastic limit cycle oscillations," *J. Fluids Struct.*, vol. 27, no. 8, pp. 1182–1198, Nov. 2011.



Noah T. Jafferis received the B.S. degree in electrical engineering from Yale University, New Haven, CT, in 2005 and the Ph.D. degree from the Department of Electrical Engineering, Princeton University, Princeton, NJ, in 2012.

He is currently a Wyss Institute Postdoctoral Fellow at Harvard University, Cambridge, MA. He was home-schooled before matriculating at Yale University at the age of 16. Some of his many research interests include micro/nanorobotics, bio-inspired engineering, 3-D integrated circuits, piezo-

electronics, 3-D printing, energy harvesting, large-area/flexible electronics, MEMS/NEMS, current density/propagation visualization, 3-D laser polymerization, robotics (including navigation, vision, and adaptive control algorithms), and brain-computer interfaces.



James C. Sturm received the B.S. degree in electrical engineering with an engineering physics certificate from Princeton University, Princeton, NJ, and the M.S.E.E. and Ph.D. degrees from Stanford University, Stanford, CA.

He is the William and Edna Macaleer Professor of Engineering and Applied Science with the Department of Electrical Engineering, Princeton University, where he has been a Professor since 1986. Since 2003, he has been the Founding Director of the Princeton Institute for the Science and Technology

of Materials, an interdisciplinary institute for education and research on a wide range of fundamental and applied fields related to advanced materials. He teaches courses on both undergraduate and graduate levels related to semiconductors and nanofabrication. Before moving to academia, he was a Microprocessor Design Engineer with Intel, Santa Clara, CA, and Siemens, Munich, Germany. In 1994–1995, he was a von Humboldt Fellow at the Institut für Halbleitertechnik, University of Stuttgart, Stuttgart, Germany. He is the cofounder of Aegis Lightwave and Suryatech and is a member of the NJ High-Tech Hall of Fame. His research focuses on the physical principles and manufacturing technology of microelectronics and optoelectronics, and his research now spans photovoltaics, large-area flexible electronics and "electronic skin," quantum computing, and the interface between medicine, biology, and nanotechnology, most recently with a focus on cancer.